JOURNAL OF SPACECRAFT AND ROCKETS
Vol. 45, No. 5, September–October 2008

Numerical Analysis of Reentry Trajectory Coupled with Magnetohydrodynamics Flow Control

Takayasu Fujino,* Tomoyuki Yoshino,† and Motoo Ishikawa‡
University of Tsukuba, Tsukuba 305-8573, Japan

DOI: 10.2514/1.33385

Effects of the magnetohydrodynamics flow control on Earth reentry flight characteristics are examined by a coupled numerical analysis of the reentry flight trajectory and the magnetohydrodynamics flows with thermochemical reactions. Initial flight altitude and velocity of a blunt body with a nose radius of 1.35 m are 75.3 km and 7.2 km/s, respectively. Numerical results show that at high altitudes such as about 75 km, the main factor of the mitigation of wall heat flux by the magnetohydrodynamics flow control is the increase of the thickness of the shock layer by applying the magnetic field. At low altitudes such as about 55 km, on the other hand, the main factor of its mitigation is the decrease of flight velocity due to the change of flight trajectory by applying the magnetic field. It can also be found from a rough estimation that about 75% of its mitigation amount at the altitude of about 60 km, where the aerodynamic heating is severest, is attributed to the decrease of flight velocity by applying the magnetic field.

Nomenclature

$\boldsymbol{B}$	=	magnetic field vector
B_r, B_z	=	components of the magnetic flux density in the r and z directions
B_0	=	magnetic flux density at the stagnation point
D_s	=	effective diffusion coefficient of species s
$\hat{D}_s$	=	average vibrational energy of molecule s, which is created or destroyed at rate $\dot{\omega}_s$
E	=	total energy
$\boldsymbol{E}$	=	electric field vector
e	=	electronic charge
$\boldsymbol{e_r}$, $\boldsymbol{e_z}$	=	unit vectors in the r and z directions
e_{ve}	=	vibrational-electronic-electron energy of species s
$e_{v,s}$	=	vibrational energy of species s
$e^*_{v,s}$	=	equilibrium vibrational energy of species s
F_G	=	gas-dynamic drag
F_M	=	magnetohydrodynamics drag
F_T	=	total drag
g	=	gravity acceleration
H	=	total enthalpy
h	=	flight altitude
h_s	=	enthalpy of species s
$h_{\mathrm{ve},s}$	=	vibrational-electronic-electron enthalpy of species s
I_s	=	first ionization energy of species s
$\boldsymbol{J}$	=	vector of electric current density
J_θ	=	component of electric current density in the θ direction
k_b	=	Boltzmann's constant
$k_{f,r}$, $k_{b,r}$	=	forward and backward reaction rate coefficients for reaction r
M	=	Mach number
M_e	=	molecular weight of an electron
M_s	=	molecular weight of species s
m	=	mass of the reentry blunt body
$\boldsymbol{m}$, $\boldsymbol{n}$	=	unit vector of the tangential and normal directions
m_e	=	mass of an electron
n_e	=	electron number density
n_s	=	number density of species s
$\dot{n}_{e,s}$	=	molar rate of production of species s by electron impact ionization
p	=	pressure
p_e	=	partial pressure of an electron
p_s	=	partial pressure of species s
Q	=	total heating
Q_{MHD}	=	magnetohydrodynamics interaction parameter
R	=	universal gas constant
R_b	=	nose radius of the body
R_e	=	Reynolds number
$R_{f,r}$, $R_{b,r}$	=	forward and backward reaction rates for reaction r
r, θ, z	=	cylindrical coordinates
S	=	surface area
T_{tr}	=	translational-rotational temperature
T_{ve}	=	vibrational-electronic-electron temperature
T_∞	=	freestream temperature
t	=	time
$\boldsymbol{u}$	=	vector of velocity
u_r, u_z	=	velocity components in the r and z directions
u_∞	=	freestream velocity
V	=	volume
v	=	flight velocity
y_s	=	mole fraction of species s
$\alpha_{s,r}$, $\beta_{s,r}$	=	forward and backward stoichiometric coefficients of species s in reaction r
γ	=	ratio of specific heat
Δ	=	shock standoff distance
ϵ_0	=	permittivity in vacuum
η_{tr}	=	mixture translational-rotational thermal conductivity
η_{ve}	=	mixture vibrational-electron thermal conductivity
θ_f	=	flight-path angle
μ	=	mixture viscosity
$\nu^m_{e,s}$	=	effective energy-exchange collision frequency of an electron with other chemical species s
ρ	=	total mass density
ρ_e	=	mass density of an electron
ρ_s	=	mass density of species s
ρ_∞	=	freestream mass density
σ	=	electrical conductivity
$\sigma^m_{e,s}$	=	effective momentum transfer cross section of electrons with neutral species s

Presented as Paper 4249 at the 38th AIAA Plasmadynamics and Lasers Conference, Miami, FL, 25–28 June 2007; received 11 July 2007; revision received 7 March 2008; accepted for publication 6 May 2008.

*Assistant Professor, Graduate School of Systems and Information Engineering. Member AIAA.
†Graduate Student, Graduate School of Systems and Information Engineering. Student Member AIAA.
‡Professor, Graduate School of Systems and Information Engineering. Senior Member AIAA.

τ = shear stress
$\tau_{i,j}$ = viscous shear stress
τ_s = translational-vibrational energy relaxation time of species s
$\dot{\omega}_s$ = mass production rate of species s
$\dot{\omega}_{ve}$ = production rate of vibrational-electronic-electron energy

I. Introduction

AS ONE of the active thermal protection techniques in Earth reentry flights, flow control with an externally applied magnetic field, herein called the magnetohydrodynamics (MHD) flow control, was proposed in the 1950s–1960s (for example, see [1–3]). On the other hand, in the 1950s–1960s, it was considered that the MHD flow control was not realistic because a very large and heavy magnet system was required for producing enough of a magnetic field to control the flows. However, a considerable development of superconducting magnet technology has been shown in more than a half-century since the MHD flow control was proposed. For example, the system of a thin superconducting magnet with the total weight of 380 kg and the strength of the magnetic field of about 1.2 T (coil diameter of 0.9 m and coil length of 1.4 m) was constructed for the balloon-borne experiment with a superconducting spectrometer to measure the energy spectrum of cosmic-ray antiprotons [the Bess–Polar program (see [4])]. The remarkable development of the magnet system allows us to reconsider the application of MHD technology to the thermal protection of reentry space vehicles.

The outline of the original idea of the MHD flow control is as follows. The Lorentz force, which is induced by applying a magnetic field to weakly ionized plasma flows in the shock layer, decelerates the flow velocity in the shock layer. Consequently, the thickness of the shock layer is increased by the MHD flow control, and then the convective heat flux can be mitigated.

The authors also numerically examined the possibility of the MHD flow control under the real reentry flight conditions of OREX at an altitude of about 60 km, where the aerodynamic heating has a peak value in the OREX trajectory, by means of numerical simulation considering the thermochemical reactions and the Hall effect [5–7]. The numerical results clearly proved the original idea of the MHD flow control and also clearly demonstrated that the Hall effect dominates the electric current distribution and results in almost no MHD effects if the wall of the vehicle is electrically conductive, but the numerical results with the Hall effect are almost the same as without the Hall effect if the wall is made of an insulator.

Recently, Bityurin et al. [8] and Otsu et al. [9] independently showed extremely interesting results by means of numerical analysis of reentry trajectories with/without the MHD flow control: applying the magnetic field leads to increasing the drag, owing to the reaction force of the Lorentz force. As a result, the MHD flow control can change the reentry flight trajectory in the direction of the reduction of the peak value of wall heat flux in the reentry flight. Otsu et al. also concluded that the mitigation of the peak value of wall heat flux by the MHD flow control is mainly due to the change of reentry flight trajectory attributed to the increase of the drag rather than due to the increase of the thickness of the shock layer. Their numerical results thus indicate that the usefulness of the MHD flow control should be discussed when considering the change of reentry flight trajectory by the MHD flow control. In the numerical studies of both Bityurin et al. [8] and Otsu et al. [9], however, the reentry flight trajectory with the MHD flow control was calculated by solving only the dynamic equation of a reentry body including the simplified models of the MHD drag without conducting a computational fluid dynamics (CFD) analysis of the MHD flows with thermochemical reactions along the reentry flight trajectory.

Although a coupled numerical analysis of the reentry trajectory and the MHD flows with thermochemical reactions involves large computational cost, the coupled numerical analysis is desired to make sure that the effects of the MHD flow control on reentry flight characteristics are under a realistic reentry flight environment. The authors have therefore conducted the coupled numerical analysis of the reentry flight trajectory and the MHD flows with thermochemical reactions. The present paper discusses the reentry flight characteristics with the MHD flow control from the results of the coupled numerical analysis.

II. Numerical Method

A. Configuration of Reentry Blunt Body and Externally Applied Magnetic Field

Figure 1 shows the configuration of a reentry blunt body. The blunt body has an axisymmetric two-dimensional (r–z) shape, which is the same as that of the blunt body used in the Orbital Reentry Experiment (OREX) in Japan (1994) [10]. The forebody shape is composed of a spherical nose with a radius of 1.35 m, a cone, and a circular shoulder. It should be noticed that the present analysis assumes an electrically insulating wall, although the electrical properties of the real OREX body are not clear.

An externally applied magnetic field is produced by a hypothetical dipole magnet with no thickness placed at the point of $r = 0$ m and $z = 0$ m inside the blunt body:

$$\boldsymbol{B}(r,z) = -\frac{B_0 R_b^3}{2(z^2+r^2)^{3/2}}\left[\left(\frac{2z^2}{z^2+r^2}-\frac{r^2}{z^2+r^2}\right)\boldsymbol{e}_z + \frac{3zr}{z^2+r^2}\boldsymbol{e}_r\right] \tag{1}$$

The present study varies the value of the parameter B_0 over a range of 0.0–0.5 T. Figure 2 depicts a distribution of the applied magnetic field around the blunt body for the parameter $B_0 = 0.5$ T.

B. Basic Equations for MHD Flows with Thermochemical Reactions

The present study regards the flowfield and the electromagnetic field as axisymmetric two-dimensional (r–z) fields. The basic equations for the MHD flows with thermochemical reactions are the mass conservation equations of chemical species, the momentum conservation equations, the total energy conservation equation, the vibrational-electronic-electron energy conservation equation, and Ohm's law. We consider the following 11 chemical species: N, O, N_2, O_2, NO, N^+, O^+, N_2^+, O_2^+, NO^+, and e^-. As a chemical nonequilibrium kinetic model, we use the Kang et al. [11] model, in which 32 chemical reactions are included. We employ Park's [12] two-temperature model to take the thermal nonequilibrium state into account. The basic equations are written as follows:

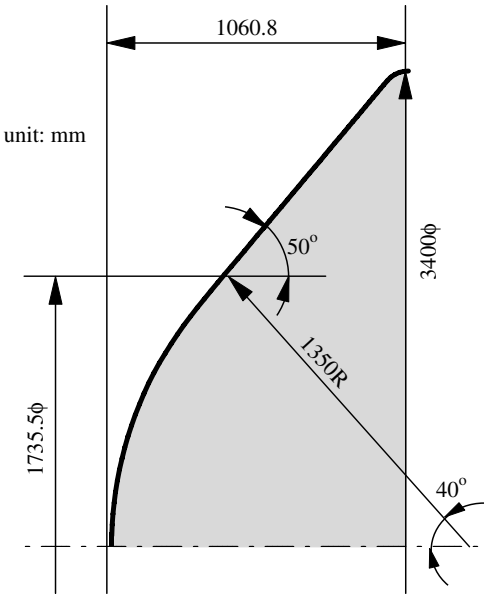

Fig. 1 Configuration of the reentry blunt body.

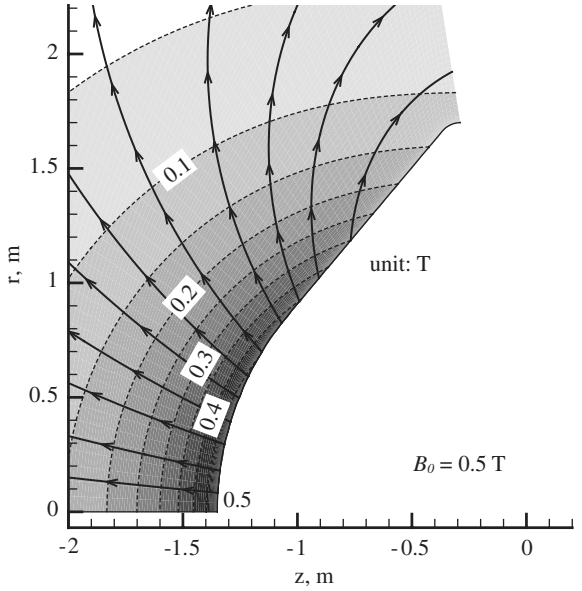

Fig. 2 Distribution of the externally applied magnetic field ahead of the blunt body for the parameter $B_0 = 0.5$ T.

Mass conservation equations of chemical species:

$$\frac{\partial \rho_s}{\partial t} + \frac{\partial}{\partial r}(\rho_s u_r) + \frac{\partial}{\partial z}(\rho_s u_z) = \dot{\omega}_s + \frac{\partial}{\partial r}\left(\rho D_s \frac{\partial y_s}{\partial r}\right) + \frac{\partial}{\partial z}\left(\rho D_s \frac{\partial y_s}{\partial z}\right) - \frac{1}{r}\left(\rho_s u_r - \rho D_s \frac{\partial y_s}{\partial r}\right) \tag{2}$$

where the total mass density ρ is given by

$$\rho = \sum_s \rho_s \tag{3}$$

The first term $\dot{\omega}_s$ on the right-hand side of Eq. (2) is the source term for the mass production rate of species s and is expressed as

$$\dot{\omega}_s = M_s \sum_{r=1}^{32} (\beta_{s,r} - \alpha_{s,r})(R_{f,r} - R_{b,r}) \tag{4}$$

The forward and backward reaction rates $R_{f,r}$ and $R_{b,r}$ are, respectively, defined by

$$R_{f,r} = k_{f,r} \prod_{s=1}^{11} (\rho_s / M_s)^{\alpha_{s,r}}, \qquad R_{b,r} = k_{b,r} \prod_{s=1}^{11} (\rho_s / M_s)^{\beta_{s,r}} \tag{5}$$

where the forward reaction rate coefficients $k_{f,r}$ and the backward reaction rate coefficients $k_{b,r}$ are tabulated in [11,13].

Momentum conservation equations:

$$\frac{\partial \rho u_r}{\partial t} + \frac{\partial}{\partial r}\left(\rho u_r^2 + p\right) + \frac{\partial}{\partial z}(\rho u_r u_z) = \frac{\partial \tau_{rr}}{\partial r} + \frac{\partial \tau_{rz}}{\partial z} + J_\theta B_z - \frac{1}{r}\left(\rho u_r^2 - \tau_{rr} + \tau_{\theta\theta}\right) \tag{6}$$

$$\frac{\partial \rho u_z}{\partial t} + \frac{\partial}{\partial r}(\rho u_z u_r) + \frac{\partial}{\partial z}(\rho u_z^2 + p) = \frac{\partial \tau_{rz}}{\partial r} + \frac{\partial \tau_{zz}}{\partial z} - J_\theta B_r - \frac{1}{r}(\rho u_r u_z - \tau_{rz}) \tag{7}$$

where the static pressure p and the viscous stress terms $\tau_{i,j}$ are defined by

$$p = \sum_s p_s = \sum_{s=1-10} \rho_s \frac{\bar{R}}{M_s} T_{\mathrm{tr}} + \rho_e \frac{\bar{R}}{M_e} T_{\mathrm{ve}} \tag{8}$$

$$\tau_{rr} = \frac{2}{3}\mu\left(2\frac{\partial u_r}{\partial r} - \frac{\partial u_z}{\partial z} - \frac{u_r}{r}\right), \qquad \tau_{\theta\theta} = \frac{2}{3}\mu\left(2\frac{u_r}{r} - \frac{\partial u_r}{\partial r} - \frac{\partial u_z}{\partial z}\right)$$
$$\tau_{zz} = \frac{2}{3}\mu\left(2\frac{\partial u_z}{\partial z} - \frac{\partial u_r}{\partial r} - \frac{u_r}{r}\right), \qquad \tau_{rz} = \tau_{zr} = \mu\left(\frac{\partial u_r}{\partial z} + \frac{\partial u_z}{\partial r}\right) \tag{9}$$

Total energy conservation equation:

$$\begin{aligned}\frac{\partial \rho E}{\partial t} + \frac{\partial}{\partial r}(\rho H u_r) + \frac{\partial}{\partial z}(\rho H u_z) &= \frac{\partial}{\partial r}\left(\eta_{\mathrm{tr}} \frac{\partial T_{\mathrm{tr}}}{\partial r} + \eta_{\mathrm{ve}} \frac{\partial T_{\mathrm{ve}}}{\partial r}\right) + \frac{\partial}{\partial z}\left(\eta_{\mathrm{tr}} \frac{\partial T_{\mathrm{tr}}}{\partial z} + \eta_{\mathrm{ve}} \frac{\partial T_{\mathrm{ve}}}{\partial z}\right) + \frac{\partial}{\partial r}\left(\rho \sum_s h_s D_s \frac{\partial y_s}{\partial r}\right) \\ &+ \frac{\partial}{\partial z}\left(\rho \sum_s h_s D_s \frac{\partial y_s}{\partial z}\right) + \frac{\partial}{\partial r}(\tau_{rr} u_r + \tau_{zr} u_z) \\ &+ \frac{\partial}{\partial z}(\tau_{rz} u_r + \tau_{zz} u_z) - \frac{\rho H u_r}{r} + \frac{\rho}{r} \sum_s h_s D_s \frac{\partial y_s}{\partial r} \\ &+ \frac{1}{r}\left(\eta_{\mathrm{tr}} \frac{\partial T_{\mathrm{tr}}}{\partial r} + \eta_{\mathrm{ve}} \frac{\partial T_{\mathrm{ve}}}{\partial r}\right) + \frac{1}{r}(\tau_{rr} u_r + \tau_{zr} u_z)\end{aligned} \tag{10}$$

where the total enthalpy H is defined as

$$H = E + \frac{p}{\rho} \tag{11}$$

Vibrational-electronic-electron energy conservation equation:

$$\begin{aligned}\frac{\partial \rho e_{\mathrm{ve}}}{\partial t} + \frac{\partial}{\partial r}(\rho e_{\mathrm{ve}} u_r) + \frac{\partial}{\partial z}(\rho e_{\mathrm{ve}} u_z) &= \dot{\omega}_{\mathrm{ve}} + \frac{\partial}{\partial r}\left(\eta_{\mathrm{ve}} \frac{\partial T_{\mathrm{ve}}}{\partial r}\right) + \frac{\partial}{\partial z}\left(\eta_{\mathrm{ve}} \frac{\partial T_{\mathrm{ve}}}{\partial z}\right) + \frac{J_\theta^2}{\sigma} \\ &+ \frac{\partial}{\partial r}\left(\rho \sum_s h_{\mathrm{ve},s} D_s \frac{\partial y_s}{\partial r}\right) + \frac{\partial}{\partial z}\left(\rho \sum_s h_{\mathrm{ve},s} D_s \frac{\partial y_s}{\partial z}\right) \\ &- \frac{1}{r}\left(\rho e_{\mathrm{ve}} u_r - \rho \sum_s h_{\mathrm{ve},s} D_s \frac{\partial y_s}{\partial r} - \eta_{\mathrm{ve}} \frac{\partial T_{\mathrm{ve}}}{\partial r}\right)\end{aligned} \tag{12}$$

where $\dot{\omega}_{\mathrm{ve}}$ is the source term for the production rate of vibrational-electronic-electron energy and is expressed as

$$\dot{\omega}_{\mathrm{ve}} = \sum_{s=\mathrm{mol}} \rho_s \frac{e_{v,s}^* - e_{v,s}}{\langle \tau_s \rangle} + 2\rho \frac{3}{2} \bar{R}(T_{\mathrm{tr}} - T_{\mathrm{ve}}) \sum_{s \neq e} \frac{\nu_{e,s}}{M_s} - \sum_{s=\mathrm{ion}} \dot{n}_{e,s} I_s + \sum_{s=\mathrm{mol}} \dot{\omega}_s \hat{D}_s - p_e\left(\frac{\partial u_r}{\partial r} + \frac{\partial u_z}{\partial z} + \frac{u_r}{r}\right) \tag{13}$$

where the relaxation time τ_s of each species for a translational-vibrational energy relaxation is calculated from the sum of the relaxation-time formula proposed by Millikan and White [14] and the correction term suggested by Park [12]. The effective energy-exchange frequency $\nu_{e,s}$ of electrons with other species is estimated by following [13]. The average vibrational energy $\hat{D}_s$, which is created or destroyed at the rate $\dot{\omega}_s$, is computed by using the nonpreferential model [13]. This model is standard in computations of reentry flows when considering thermochemical reactions, although the use of this model is not consistent because this model is the separate model of nonequilibrium dissociation rates and vibrational energy transfer from chemical reactions. The authors will examine the self-consistent model [15] in a future work.

The transport coefficients such as the effective diffusion coefficient of each species D_s, the mixture viscosity μ, the mixture translational-rotational thermal conductivity η_{tr}, and the mixture vibrational-electron thermal conductivity η_{ve} are estimated by an extension model of Yos's formulas for the multitemperature gas mixture (see [13]).

Ohm's law:

$$\boldsymbol{J} = \sigma(\boldsymbol{E} + \boldsymbol{u} \times \boldsymbol{B}) \tag{14}$$

The term of the Hall effect is not included in Eq. (14), because our previous study [5–7], which treats the highest wall heat flux at the altitude of about 60 km, has clearly shown that the Hall effect dominates the electric current distribution and results in almost no MHD effects if the wall of the vehicle is electrically conductive, but the numerical results with the Hall effect are almost the same as without the Hall effect if the wall is made of an insulator. Therefore, the present analysis assumes that the wall is made of an insulator and the enormous computational cost can be avoided. The ratio of the ion-slip coefficient and the Hall parameter is proportional to the square root of the mass ratio, and therefore the effect of ion slip is much smaller than the Hall effect. As aforementioned, the Hall effect can be neglected if we assume the insulator wall, and we can also neglect the ion-slip effect. At much higher altitude, however, it is not clear whether or not the Hall effect can be neglected even if the insulator wall is assumed, and therefore we have decided that the highest altitude is 75.3 km in our flight-trajectory analysis. These effects at much higher altitude will be examined in the near future. Because of the assumption of the axisymmetric two-dimensional (r–z) electromagnetic field and the neglect of the Hall effect and the ion-slip effect, the electric field $\boldsymbol{E}$ is not induced. Consequently, the electric current density has only the azimuthal θ component, which is expressed as

$$J_\theta = \sigma(u_z B_r - u_r B_z) \tag{15}$$

where the electrical conductivity σ is written as

$$\sigma = \frac{n_e e^2}{m_e \sum_{s \neq e} \nu_{e,s}^m} \tag{16}$$

The effective momentum transfer collision frequency $\nu_{e,s}^m$ of electrons with the other chemical species s is written as

$$\nu_{e,s}^m = \begin{cases} 6\pi \left(\frac{e^2}{12\pi\epsilon_0 k_b T_{\mathrm{ve}}} \right)^2 \ln\left[12\pi \left(\frac{\epsilon_0 k_b}{e^2} \right)^{3/2} \sqrt{\frac{T_{\mathrm{ve}}^3}{n_e}} \right] n_s \sqrt{\frac{8 k_b T_{\mathrm{ve}}}{\pi m_e}} & \text{if } s \text{ is ion species} \\ \frac{4}{3} \sigma_{e,s}^m n_s \sqrt{\frac{8 k_b T_{\mathrm{ve}}}{\pi m_e}} & \text{otherwise} \end{cases} \tag{17}$$

where the effective momentum transfer cross section of electrons with the other neutral chemical species s $\sigma_{e,s}^m$ is computed using the curve fit presented in [13].

C. Numerical Procedures and Validation of CFD Code

The conservation equations for the MHD flows are transformed into the generalized coordinate system. The convection terms are calculated by the advection upstream splitting method (AUSM)-DV [16] coupled with the fourth-order compact MUSCL total-variation-diminishing (TVD) scheme [17]. The viscous terms are calculated by the second-order central-differencing scheme. The time integration is performed by the lower/upper symmetric Gauss–Seidel scheme [18]. The present CFD analysis uses the no-slip condition, the noncatalytic wall condition, and the radiative equilibrium temperature condition on the wall boundary. The surface emissivity coefficient used in the radiative equilibrium temperature condition is set to 0.84, referring to [19]. The translational-rotational temperature and the vibrational-electronic-electron temperature on the wall surface are assumed to be in equilibrium with the radiative equilibrium wall temperature. It is well known that the prediction of wall heat flux is extremely sensitive to the computational grid, especially the grid spacing near the wall surface. We therefore checked the grid dependency in advance. Based on the check, a proper computational grid is employed in the present study. The grid spacing near the wall is about 2–3 μm.

As presented in [20], the authors have computed hypersonic flows around a body without MHD interaction under Lobb's [21] experimental condition, and the computed shock standoff distance has also been compared with Lobb's experimental result for validating numerical methods and thermochemical models in our developed CFD code. The shock standoff distance is a sensitive measure of the accuracy of numerical models and methods because it is directly influenced by the density distribution between the shock wave and the body surface, which is affected by thermochemical properties. The computational results have demonstrated that there is an excellent agreement between the computational result and the experimental result in the shock standoff distance.

To validate our numerical code, we have compared our numerical results with the simulation results of Poggie and Gaitonde [22]. Figure 3a shows the comparison of pressure distribution in the case of the MHD interaction $Q_{\mathrm{MHD}} = 0$ and 6, which is defined as $Q_{\mathrm{MHD}} = \sigma B_0^2 R_b / \rho_\infty u_\infty$. Figure 3b also compares the two results of the relation of shock standoff distance and the MHD interaction parameter Q_{MHD}. Both figures indicate that our results are almost the same as Poggie and Gaitonde's results.

D. Numerical Method and Validation of Reentry Flight Trajectory

The MHD flows and the reentry flight trajectory are calculated alternately for examining effects of the MHD flow control on the reentry flight trajectory. The present study assumes that the blunt body enters into the atmosphere at the attack angle of zero and also that the lift is zero. Referring to the OREX reentry experiments [10], the mass of the reentry blunt body m is set to 761 kg and the flight-path angle θ_f is fixed to 3 deg.

The dynamic equations of the blunt body for computing the reentry flight trajectory are written as follows:

$$m \frac{\mathrm{d}v}{\mathrm{d}t} = -F_T + mg \sin\theta_f \tag{18}$$

$$\frac{\mathrm{d}h}{\mathrm{d}t} = -v \sin\theta_f \tag{19}$$

where the total drag F_T, which is evaluated from the results of CFD analysis of the MHD flows, is the sum of the gas-dynamic drag F_G and the MHD drag F_M, as follows:

$$F_T = F_G + F_M \tag{20}$$

$$F_G = z \text{ component of } \left[-\iint p\boldsymbol{n}\,\mathrm{d}S + \iint \tau \boldsymbol{m}\,\mathrm{d}S \right] \tag{21}$$

$$F_M = z \text{ component of } \left[\iiint \boldsymbol{J} \times \boldsymbol{B}\,\mathrm{d}V \right] \tag{22}$$

The dynamic equations of the blunt body are integrated with time by the Euler explicit method. The time step is set to be 2.0 s. Initial

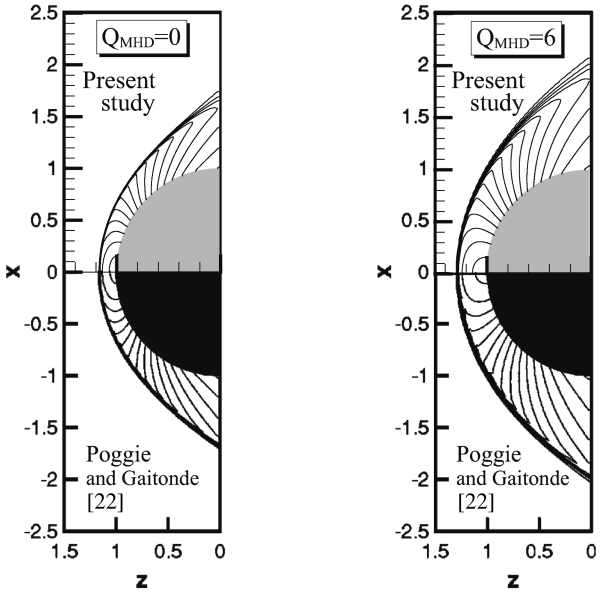

a) Pressure distribution

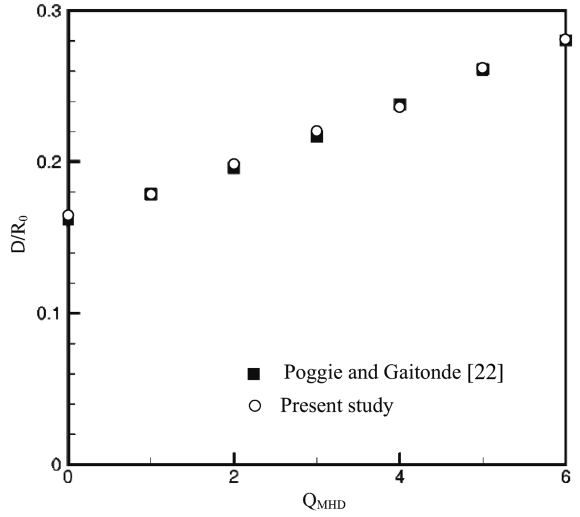

b) Shock standoff distance

Fig. 3 Comparison of the authors' and Poggie and Gaitonde's [22] numerical results: a) pressure distribution and b) shock standoff distance.

flight conditions are as follows: the altitude is 75.3 km and the flight velocity is 7.2 km/s. The coupled analysis of the reentry flight trajectory and the MHD flows is terminated when the blunt body reaches the altitude of 45 km, where the aerodynamic heating becomes very small and the gas in the shock layer has no electrical conductivity.

Figure 4 illustrates a good agreement between the OREX experimental result and the present numerical result as for the relation between the altitude and the flight velocity along a normal flight trajectory ($B_0 = 0.0$ T) at altitudes from 75 to 60 km, where the large effect of MHD interaction can be expected because of high electrical conductivity. This fact indicates that the present numerical modeling can give a reasonable result at altitudes from 75 to 60 km. At altitudes below about 55 km, however, there is a discrepancy between the experimental result and the present numerical result, as can be also found from Fig. 4. The reason of the discrepancy is not clear and further study is required.

III. Results and Discussion

First, numerical results of the MHD flow control under the initial flight conditions (the flight altitude of 75.3 km and the flight velocity

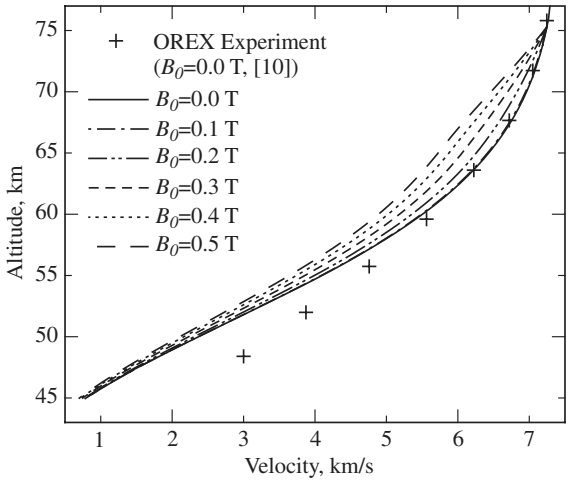

Fig. 4 Relation of flight velocity and flight altitude for the parameter $B_0 = 0.0$ to 0.5 T.

of 7.2 km/s) will be briefly shown to clarify the effects of applying a magnetic field on the flowfield, the wall heat flux, and the drag acting on the blunt body. Then effects of the MHD flow control on the flight characteristics along the reentry trajectory will be discussed.

Figure 5 depicts pressure distributions around the blunt body under the initial flight conditions for the applied magnetic field of the parameter $B_0 = 0.0$ to 0.5 T. This figure demonstrates that the thickness of the shock layer increases with the strength of the applied magnetic field.

Figure 6 illustrates distributions of electrical conductivity for $B_0 = 0.0$ and 0.5 T. When the magnetic field is not applied ($B_0 = 0.0$ T), the weakly ionized plasma is produced by thermal ionizations attributed to the bow shock wave. As shown in Fig. 6a, therefore, the electrical conductivity for $B_0 = 0.0$ T has the maximum value near the stagnation line behind the bow shock wave, where the influence of the bow shock wave on the flowfield becomes the strongest. On the other hand, it can be found from Fig. 6b that the electrical conductivity for $B_0 = 0.5$ T has the maximum value in the area distant from the stagnation line, where the large azimuthal electric current density is induced by applying the magnetic field, as illustrated in Fig. 7. The Joule heating attributed to the azimuthal

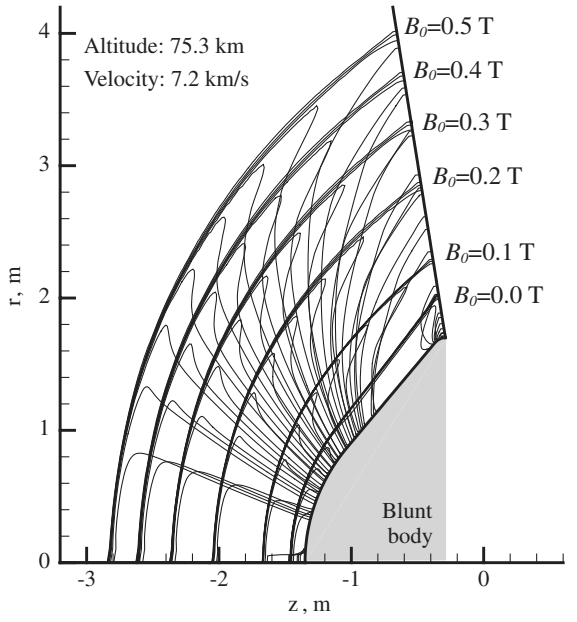

Fig. 5 Two-dimensional (r–z) distributions of pressure for the parameter $B_0 = 0.0$ to 0.5 T under the initial flight conditions (the flight altitude: 75.3 km and the flight velocity: 7.2 km/s).

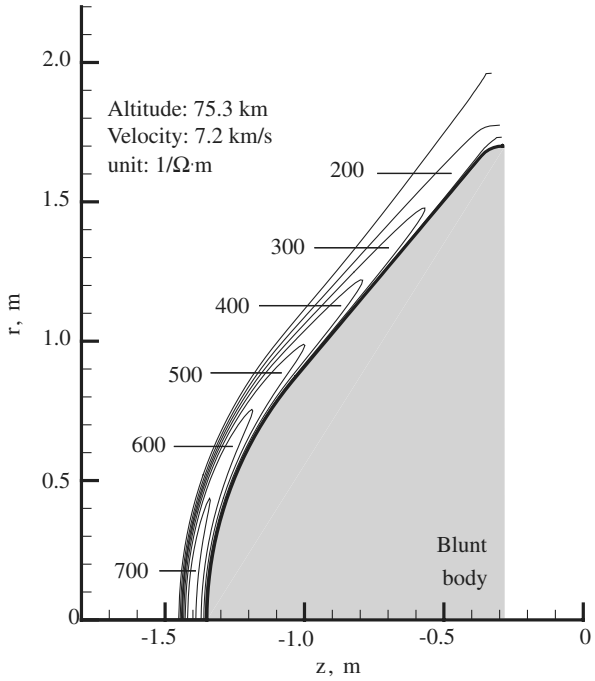

a) B_0=0.0 T

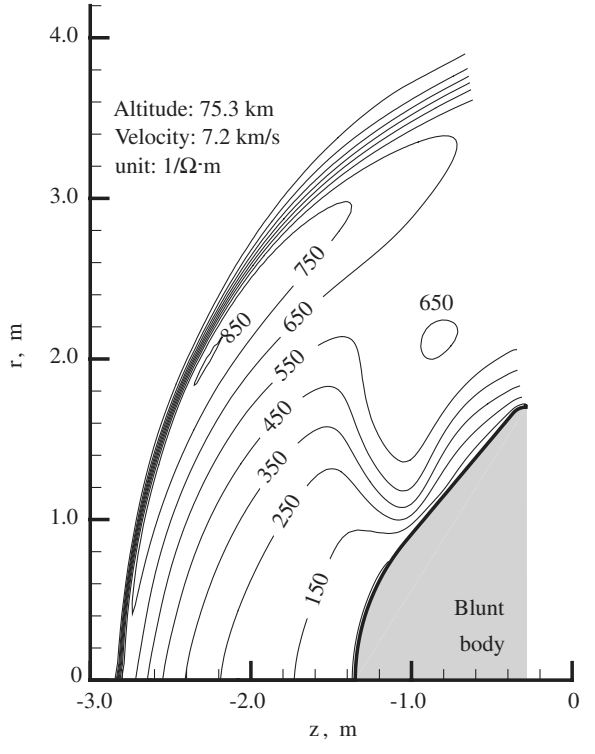

b) B_0=0.5 T

Fig. 6 Two-dimensional (r–z) distributions of electrical conductivity for the parameter (a) $B_0 = 0.0$ T and (b) $B_0 = 0.5$ T under the initial flight conditions (the flight altitude: 75.3 km and the flight velocity: 7.2 km/s).

electric current density causes the vibrational-electronic-electron temperature to become higher than with the case of $B_0 = 0.0$ T. The enhancement of ionization reactions owing to the rise of the vibrational-electronic-electron temperature results in the maximum electrical conductivity for the parameter $B_0 = 0.5$ T being higher than that for the parameter $B_0 = 0.0$ T, as shown in Fig. 6.

Distributions of wall heat flux for the parameter $B_0 = 0.0$ to 0.5 T are illustrated in Fig. 8. By increasing the strength of the applied

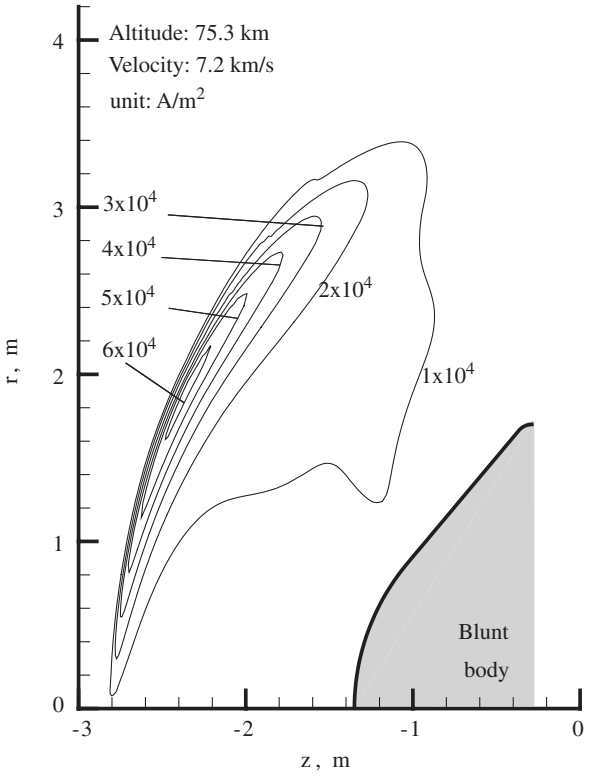

Fig. 7 Two-dimensional (r–z) distribution of azimuthal electric current density for the parameter $B_0 = 0.5$ T under the initial flight conditions (the flight altitude: 75.3 km and the flight velocity: 7.2 km/s).

magnetic field, the thickness of the shock layer increases, which results in the decrease of the wall heat flux. The wall heat flux at the stagnation point for $B_0 = 0.5$ T is 53% of its value obtained for $B_0 = 0.0$ T.

Figure 9 shows influences of the strength of the applied magnetic field on the total drag F_T, the gas-dynamic drag F_G, and the MHD drag F_M under the initial flight conditions. The MHD drag F_M increases with the strength of the magnetic field due to the increase in the Lorentz force. On the other hand, the gas-dynamic drag F_G decreases with increasing the strength of the applied magnetic field. This is because the gas velocity in the shock layer becomes lower with increasing the strength of the applied magnetic field, so that the dynamic pressure becomes lower with increasing the strength of the applied magnetic field. The total drag F_T, which is sum of the gas-

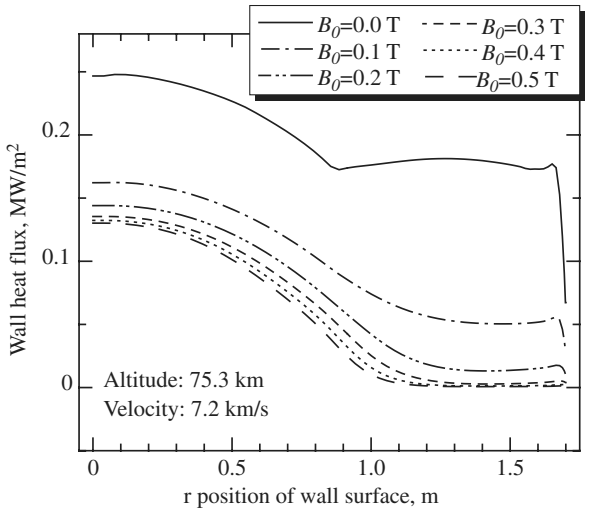

Fig. 8 Distributions of wall heat flux for the parameter $B_0 = 0.0$ to 0.5 T under the initial flight conditions (the flight altitude: 75.3 km and the flight velocity: 7.2 km/s).

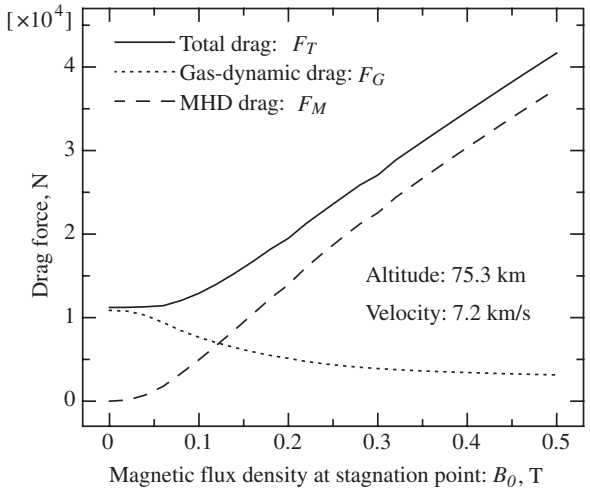

Fig. 9 Total drag F_T, gas-dynamic drag F_G, and MHD drag F_M for the parameter $B_0 = 0.0$ to 0.5 T under the initial flight conditions (the flight altitude: 75.3 km and the flight velocity: 7.2 km/s).

dynamic drag F_G and the MHD drag F_M, increases with the strength of the applied magnetic field. This is because the total drag F_T is dominated by the MHD drag F_M, as can be found from Fig. 9. The total drag F_T for $B_0 = 0.5$ T is about quadruple of that without applying the magnetic field ($B_0 = 0.0$ T).

Hereafter, effects of the MHD flow control on the flight characteristics along the reentry trajectory will be discussed. It can be found from Fig. 4 that the flight velocity at the same altitude decreases with increasing the strength of the applied magnetic field. At altitudes above about 65 km, the difference in flight velocity with and without applying the magnetic field is large compared with low altitudes. Its difference becomes the largest at the altitude of about 65 km under any applied magnetic field condition, and then at altitudes below about 65 km, its difference becomes smaller as the altitude decreases. The difference in the flight velocity for $B_0 = 0.0$ and 0.5 T is about 0.7 km/s at the altitude of 65 km and is 0.1 km/s or less at the altitudes lower than 50 km.

Table 1 shows the flight time at altitudes from 75.3 to 45 km for the parameter $B_0 = 0.0$ to 0.5 T. As the strength of the applied magnetic field increases, the flight time becomes longer. This is because the flight velocity at the same altitude becomes lower with increasing the strength of the applied magnetic field. The flight time for $B_0 = 0.5$ T is about 19 s longer than that for $B_0 = 0.5$ T.

Figure 10 illustrates distributions of the total drag F_T, the gas-dynamic drag F_G, and the MHD drag F_M along altitudes for the parameter $B_0 = 0.0$ to 0.5 T. At altitudes above about 65 km, the total drag F_T increases with the strength of the applied magnetic field. This result leads to the fact that at altitudes above about 65 km, the difference in flight velocity with and without applying the magnetic field at the same altitude becomes larger with increasing the strength of the applied magnetic field, as shown in Fig. 4. As can be found from the comparison of the gas-dynamic drag F_G (Fig. 10b) and the MHD drag F_M (Fig. 10c), the increase of total drag F_T (Fig. 10a) with the strength of the applied magnetic field at altitudes above 65 km is attributed to the increase of MHD drag F_M. At altitudes below about 65 km, on the other hand, the total drag F_T with applying the magnetic field is smaller than that without it under any applied magnetic field conditions, and the stronger the applied magnetic field, the smaller the total drag F_T becomes. At altitudes below about

Table 1 Flight times and total heating Q at altitudes from about 75 to 45 km for the parameter $B_0 = 0.0$ to 0.5 T

B_0, T	0.0	0.1	0.2	0.3	0.4	0.5
Flight time, s	162.3	162.8	166.2	171.8	177.0	181.5
Total heating Q, MJ	299.0	263.6	228.7	215.2	193.2	178.5
$Q/Q_{B_0=0.0\ \mathrm{T}}$	1	0.88	0.76	0.72	0.65	0.60

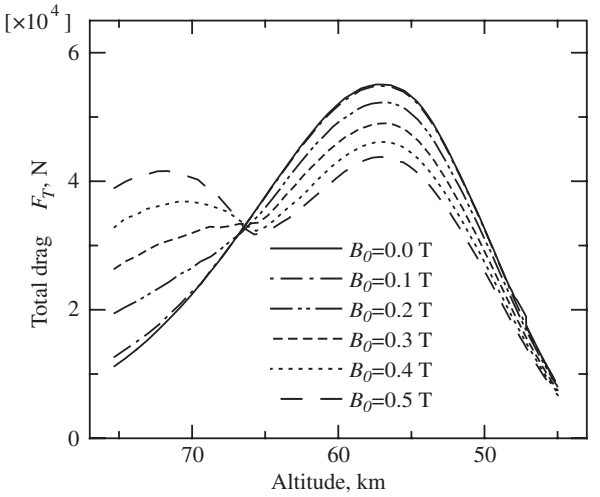

a) Total drag F_T

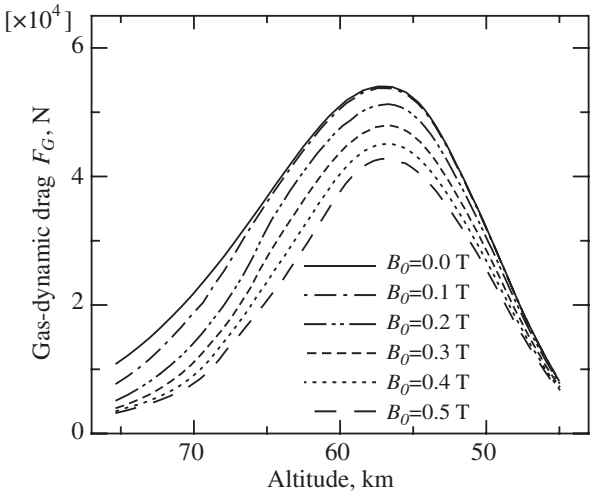

b) Gas-dynamic drag F_G

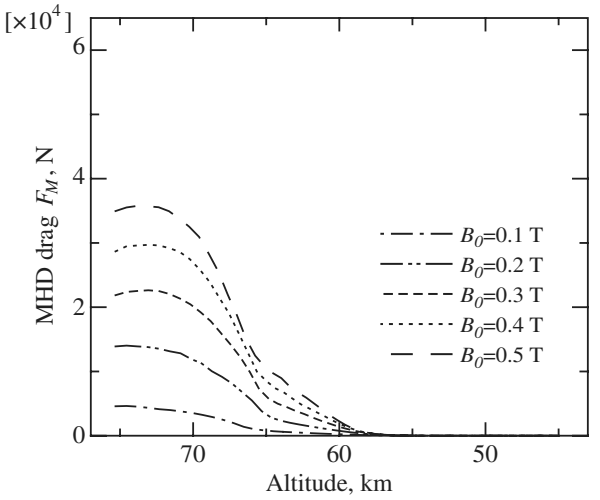

c) MHD drag F_M

Fig. 10 Distributions of total drag F_T, gas-dynamic drag F_G, and MHD drag F_M along altitudes for the parameter $B_0 = 0.0$ to 0.5 T.

65 km, therefore, the difference in flight velocity with and without applying the magnetic field becomes smaller as the flight altitude decreases, and also the differences of flight velocity among the applied magnetic field conditions become smaller, as shown in Fig. 4. It can be found from the comparison of the gas-dynamic drag F_G (Fig. 10b) and the MHD drag F_M (Fig. 10c) that the total drag F_T

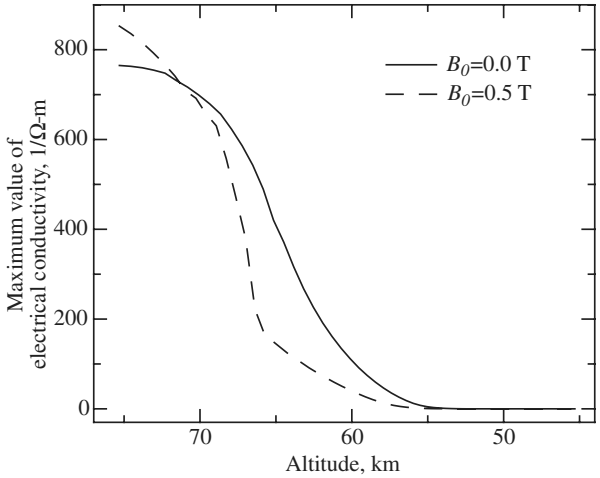

Fig. 11 Relation between flight altitude and maximum value of electrical conductivity for the parameter $B_0 = 0.0$ and 0.5 T.

(Fig. 10a) is dominated by the gas-dynamic drag F_G under any applied magnetic field condition at altitudes below about 65 km. Figure 10b shows that the gas-dynamic drag F_G with applying the magnetic field is smaller than that without applying it at all flight altitudes, and also the gas-dynamic drag F_G decreases with increasing the strength of the applied magnetic field. At the altitudes above about 55 km, the decrease of gas-dynamic drag F_G is caused both by the decrease of flight velocity by applying the magnetic field (Fig. 4) and by the decrease of the flow velocity in the shock layer by applying it (Fig. 9). At the altitudes below about 55 km, however, the decrease of gas-dynamic drag F_G is caused mainly by the decrease of flight velocity by applying the magnetic field. There is little influence of the applied magnetic field on the flow velocity in the shock layer at the altitude below about 55 km, where the electrical conductivity in the shock layer becomes almost zero for any applied magnetic field condition, as will be shown in Fig. 11.

Figure 11 depicts the relation between the flight altitude and the maximum value of electrical conductivity in the shock layer for the parameter $B_0 = 0.0$ and 0.5 T. The electrical conductivity in the shock layer decreases with decreasing the altitude under any applied magnetic field condition, and then the electrical conductivity becomes almost zero at altitudes below about 55 km. Similar results are also obtained for all other applied magnetic field conditions. The MHD drag F_M therefore becomes smaller with decreasing the altitude, and the MHD drag F_M is almost zero at altitudes below about 55 km, as shown in Fig. 10c.

It can be also found from Fig. 11 that the maximum value of electrical conductivity for $B_0 = 0.5$ T is higher than that for $B_0 = 0.0$ T at the altitudes above about 72 km. This is, as has been explained from Fig. 6, because the vibrational-electronic-electron temperature is raised by the large Joule heating attributed to the strong MHD interaction, so that the ionization reaction is enhanced. On the other hand, at altitudes below about 72 km, the maximum electrical conductivity for $B_0 = 0.5$ T is lower than that for $B_0 = 0.0$ T, as shown in Fig. 11. Figure 12 depicts two-dimensional distributions of electrical conductivity for the parameter $B_0 = 0.0$ and 0.5 T at the altitude of 65.1 km. Under both applied magnetic field conditions, the electrical conductivity has the maximum value near the stagnation line behind the bow shock wave. It is also noted in Fig. 12 that the electrical conductivity in the shock layer for $B_0 = 0.5$ T is overall lower than that for $B_0 = 0.0$ T. This is because of the following two reasons: one is that the Joule heating for $B_0 = 0.5$ T at the altitude of 65.1 km is significantly smaller than with the altitude of about 75.3 km, and the other is that the strength of the bow shock wave for $B_0 = 0.5$ T is weaker than that for $B_0 = 0.0$ T due to the reduction of flight velocity by applying the magnetic field. These two reasons also explain that the electrical conductivity in the shock layer for $B_0 = 0.5$ T is smaller than that for the parameter $B_0 = 0.0$ T at the altitudes below about 72 km, as shown in Fig. 11.

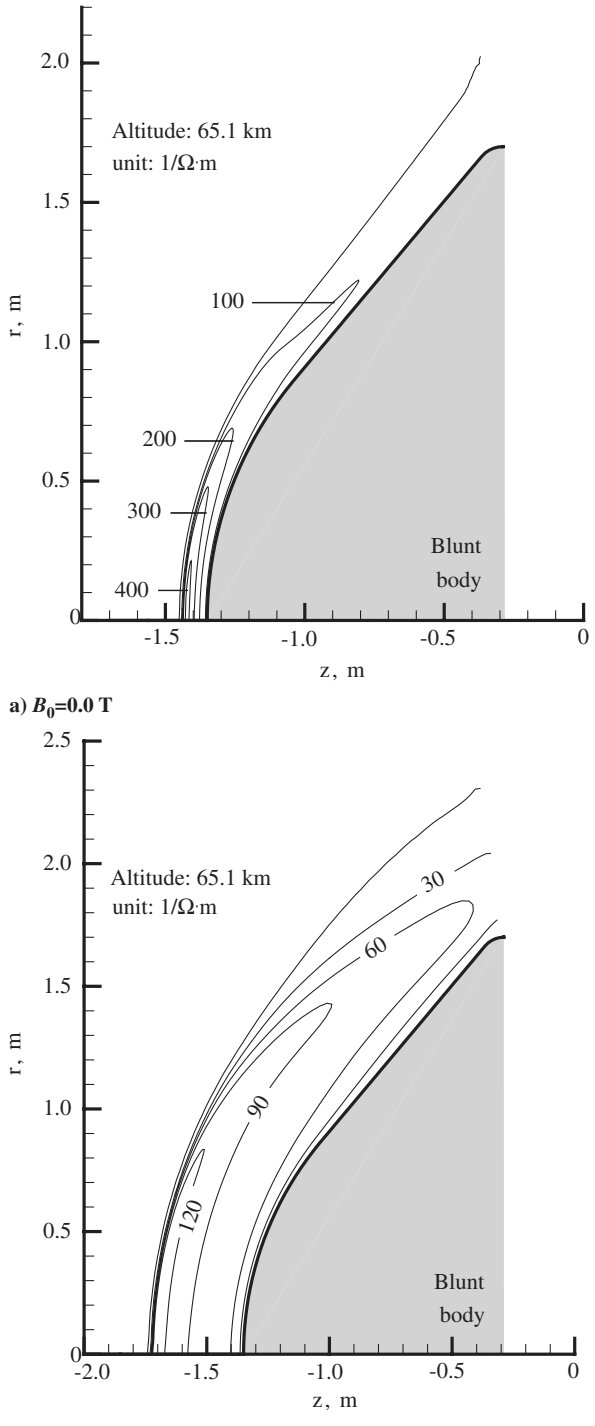

Fig. 12 Two-dimensional (r–z) distributions of electrical conductivity for the parameter a) $B_0 = 0.0$ T and b) $B_0 = 0.5$ T at the altitude of 65.1 km.

Figure 13 depicts the relation between the flight altitude and the wall heat flux at the stagnation point for the parameter $B_0 = 0.0$ to 0.5 T. Under any applied magnetic field condition, the wall heat flux at the stagnation point has a peak value at about 60 km. As the applied magnetic field becomes stronger, the wall heat flux at the stagnation point at the same altitude becomes lower, and also its peak value along the reentry trajectory becomes lower: its peak value for $B_0 = 0.5$ T is about 73% of its value for $B_0 = 0.0$ T. The mitigation of wall heat flux by applying the magnetic field is caused from the following two factors: 1) the increase of the thickness of the shock layer (Figs. 5 and 8) and 2) the decrease of flight velocity due to the change of flight trajectory (Fig. 4). To roughly estimate the degree of contribution of

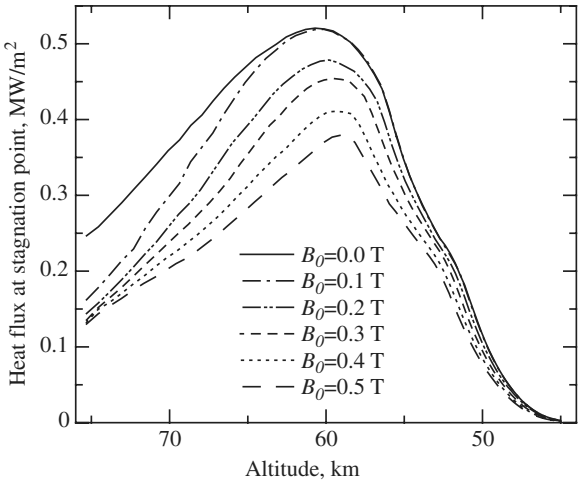

Fig. 13 Relation between flight altitude and heat flux at the stagnation point for the parameter $B_0 = 0.0$ to 0.5 T.

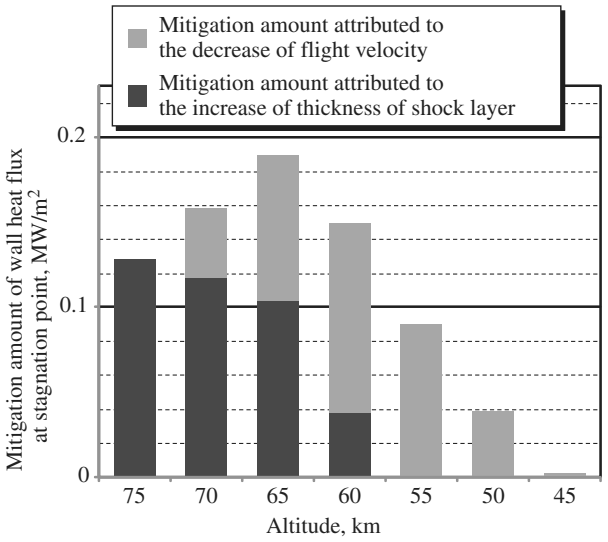

Fig. 14 Contribution of the two factors to the mitigation of wall heat flux for the parameter $B_0 = 0.5$ T.

the two factors to the mitigation of wall heat flux, the authors conducted a series of computations without applying the magnetic field under the flight conditions corresponding to the flight trajectory for $B_0 = 0.5$ T, and then both results were compared. Figure 14 illustrates the contribution of the two factors to the mitigation of wall heat flux at the stagnation point for the $B_0 = 0.5$ T. At high altitudes, such as at about 75 km, the main mitigating factor of wall heat flux by applying the magnetic field of the parameter $B_0 = 0.5$ T is the increase of the thickness of the shock layer caused by applying the magnetic field. At low altitudes such as at about 55 km, on the other hand, the main mitigating factor is the decrease of flight velocity due to the change of flight trajectory by applying the magnetic field. At the altitude of about 60 km, where the wall heat flux at the stagnation point has a peak value, about 75% of the whole mitigation amount of wall heat flux at the stagnation point for the parameter $B_0 = 0.5$ T is attributed to the decrease of flight velocity due to the change of flight trajectory.

Table 1 shows the total aerodynamic heating Q at altitudes from about 75 to 45 km for the parameter $B_0 = 0.0$ to 0.5 T. The total aerodynamic heating Q is defined as

$$Q = \int_{T_{\text{flight}}} \left[\int_{S_{\text{wall}}} q_{\text{wall}} \, \mathrm{d}S \right] \mathrm{d}t \tag{23}$$

where q_{wall} is the wall heat flux, T_{flight} is the flight time at altitudes from 75.3 to 45 km (see Table 1), and S_{wall} is the area of wall surface. It can be found from Table 1 that the total heating can be reduced by the MHD flow control although the flight time is increased by the MHD flow control, and also that the total heating becomes lower with increasing the strength of the applied magnetic field. The total aerodynamic heating for $B_0 = 0.5$ T becomes about 60% of its value without applying magnetic field ($B_0 = 0.0$ T).

IV. Conclusions

The effects of the MHD flow control on the flight characteristics along the reentry trajectory have been examined by means of the coupled numerical analysis of the reentry flight trajectory and the MHD flows with thermochemical reactions. The main results are summarized as follows.

1) The MHD flow control results in the mitigation of the peak value of wall heat flux at the stagnation point in the reentry flight by the two factors: one is the increase of thickness of the shock layer by applying the magnetic field, and the other is the decrease of flight velocity attributed to the change of flight trajectory by applying the magnetic field. When the magnetic field with the strength of about 0.5 T is applied, the peak value of wall heat flux at the stagnation point is mitigated to about 73% of the peak value obtained without applying the magnetic field, and about 75% of the whole mitigation amount is attributed to the decrease of flight velocity due to the change of flight trajectory.

2) At high altitudes such as at about 75 km, the main factor of the mitigation of wall heat flux by applying the magnetic field is the increase of the thickness of the shock layer by the Lorentz force. At low altitudes such as at about 55 km, on the other hand, the main factor of its mitigation is the decrease of flight velocity due to the change of flight trajectory.

3) Although the flight time is increased by the MHD flow control, the total heating integrated over the flight trajectory can be significantly reduced by the MHD flow control. When the magnetic field with the strength of about 0.5 T is applied, the total aerodynamic heating at altitudes from about 75 to 45 km can be reduced to about 60% of its value obtained without applying magnetic field.

It may be possible that the peak value of wall heat flux at the stagnation point and the total heating in reentry flights with applying the magnetic field strongly depend on the flight altitude at which the application of the magnetic field starts. The authors will examine influences of the altitude at which the application of the magnetic field starts on the usefulness of the MHD flow control in a near-future study. The present analysis neglected the Hall effect and the ion-slip effect because the insulating wall was assumed. These effects may considerably influence the usefulness of the MHD flow control at higher altitudes. These effects at higher altitude will therefore be studied in ongoing work.

Acknowledgments

This study was partly supported by University of Tsukuba Research Project. The authors would like to thank J. Kasahara (University of Tsukuba), H. Otsu (Shizuoka University), I. Funaki [Japan Aerospace Exploration Agency (JAXA)], A. Matsuda (JAXA), and T. Abe (JAXA) for useful discussion.

References

[1] Meyer, R. C., "On Reducing Aerodynamic Heat-Transfer Rates by Magnetohydrodynamic Techniques," *Journal of the Aero/Space Sciences*, Vol. 25, No. 9, 1958, pp. 561–566, 572.

[2] Bush, W. B., "Magnetohydrodynamic-Hypersonic Flow Past a Blunt Body," *Journal of the Aero/Space Sciences*, Vol. 25, No. 11, 1958, pp. 685–690, 728.

[3] Ziemer, R. W., "Experimental Investigation in Magneto-Aerodynamics," *American Rocket Society Journal*, Vol. 29, No. 19, 1959, pp. 642–647.

[4] Yamamoto, A., "A Thin Superconducting Solenoid Magnet for Astroparticle Physics," *Nuclear Physics B, Proceedings Supplements*, Vol. 113, Dec. 2002, pp. 299–302. doi:10.1016/S0920-5632(02)01855-8

[5] Fujino, T., Funaki, I., Sugita, H., Mizuno, M., and Ishikawa, M., "Influences of Electrical Conductivity of Wall on Magnetohydrodynamic Control of Aerodynamic Heating," *Journal of Spacecraft and Rockets*, Vol. 43, No. 1, 2006, pp. 63–70. doi:10.2514/1.13770

[6] Fujino, T., and Ishikawa, M., "Numerical Studies of the Magnetohydrodynamic Flow Control Considering Real Wall Electrical Conductivity," *Journal of Spacecraft and Rockets*, Vol. 44, No. 3, 2007, pp. 625–632. doi:10.2514/1.25824

[7] Fujino, T., Funaki, I., Sugita, H., Mizuno, M., and Ishikawa, M.,"Numerical Studies of Influences of Hall Effect on MHD Flow Control Around Blunt Body OREX,"AIAA Paper 2004–2561, June 2004.

[8] Bityurin, V. A., and Bocharov, A. N., "MHD Flow Control in Hypersonic Flight," *Proceedings of the Fifteenth International Conference on MHD Energy Conversion and Sixth international Workshop on Magnetoplasma Aerodynamics*, Vol. 2, Inst. of High Temperatures, Russian Academy of Sciences, Moscow, 2005, pp. 429–433.

[9] Otsu, H., Atsushi, M., Takashi, A., and Konigorski, D., "Feasibility Study on the Flight Demonstration for a Reentry Vehicle with the Magnetic Flow Control," AIAA Paper 2006–3566, June 2006.

[10] Yamamoto, Y., "Recent Comparisons of Aerothermodynamic Results by CFD and FEM Coupling Analysis with OREX Flight Experiments," *Proceedings of the Thirteenth National Aerospace Laboratory Symposium on Aircraft Computational Aerodynamics*, National Aerospace Lab. of Japan, Tokyo, 1995, pp. 27–39.

[11] Kang, S. W., Jones, W. L., and Dunn, M. G., "Theoretical and Measured Electron-Density Distributions at High Altitudes," *AIAA Journal*, Vol. 11, No. 2, 1973, pp. 141–149. doi:10.2514/3.50446

[12] Park, C., "Assessment of Two–Temperature Kinetic Model for Ionizing Air," *Journal of Thermophysics and Heat Transfer*, Vol. 3, No. 3, 1989, pp. 233–244. doi:10.2514/3.28771

[13] Gnoffo, P. A., Gupta, R. N., and Shinn, J. L., "Conservation Equations and Physical Models for Hypersonic Air Flows in Thermal and Chemical Nonequilibrium," NASA TP-2867, Feb. 1989.

[14] Millikan, R. C., and White, D. R., "Systematics of Vibrational Relaxation," *Journal of Chemical Physics*, Vol. 39, No. 12, 1963, pp. 3209–3213. doi:10.1063/1.1734182

[15] Seror, S., Druguet, M. C., Schall, E., and Zeitoun, D. E., "Coupled Vibration-Dissociation-Exchange Reactions Model for Hypersonic Airflow Computations," *AIAA Journal*, Vol. 36, No. 4, 1998, pp. 532–538.

[16] Wada, Y., and Liou, M-S., "A Flux-Splitting Scheme with High-Resolution and Robustness for Discontinuities," AIAA Paper 94-0083, Jan. 1994.

[17] Yamamoto, S., "Shock-Vortex Capturing Method and Its Application to Unsteady 3-D Cascade Flow," *Computational Fluid Dynamics Journal*, Vol. 8, No. 2, 1999, pp. 341–349.

[18] Yoon, S., and Jameson, A., "Lower-Upper Symmetric-Gauss-Seidel Method for the Euler and Navier-Stokes Equations," *AIAA Journal*, Vol. 26, No. 9, 1988, pp. 1025–1026. doi:10.2514/3.10007

[19] Ishida, K., Sano, M., Hamamura, O., and Sakuyama, H., "Emittance Measurement of BHE Coating on Refractory Tiles," National Aerospace Lab. TR-1320, Tokyo, Feb. 1997 (in Japanese).

[20] Fujino, T., Funaki, I., Sugita, H., Mizuno, M., and Ishikawa, M., "Numerical Analyses on Flow Control around Blunt Body 'OREX' by Magnetic Field," AIAA Paper 2003-3760, June 2003.

[21] Lobb, R. K., "Experimental Measurement of Shock Detachment Distance on Spheres Fired in Air at Hypervelocities," *The High Temperature Aspects of Hypersonic Flow*, edited by C. W. Nelson, Pergamon, New York, 1964, pp. 519–527.

[22] Poggie, J., and Gaitonde, D. V., "Magnetic Control of Flow Past a Blunt Body: Numerical Validation and Exploration," *Physics of Fluids*, Vol. 14, No. 5, 2002, pp. 1720–1731. doi:10.1063/1.1465424

A. Ketsdever
Associate Editor